

Transport Between Twisted Graphene Layers

R. Bistritzer and A.H. MacDonald¹

¹*Department of Physics, The University of Texas at Austin, Austin Texas 78712*

(Dated: September 21, 2018)

Commensurate-incommensurate transitions are ubiquitous in physics and are often accompanied by intriguing phenomena. In few-layer graphene (FLG) systems, commensurability between honeycomb lattices on adjacent layers is regulated by their relative orientation angle θ , which is in turn dependent on sample preparation procedures. Because incommensurability suppresses inter-layer hybridization, it is often claimed that graphene layers can be electrically isolated by a relative twist, even though they are vertically separated by a fraction of a nanometer. We present a theory of interlayer transport in FLG systems which reveals a richer picture in which the specific conductance depends sensitively on θ , single-layer Bloch state lifetime, in-plane magnetic field, and bias voltage. We find that linear and differential conductances are generally large and negative near commensurate values of θ , and small and positive otherwise.

Experimental advances in the fabrication of graphene-based structures[1, 2] have now provided researchers with a multitude of systems that have strikingly distinct electronic properties. By engineering the substrate underlying exfoliated samples [3–5], identifying exfoliated fragments with folds[6], or controlling epitaxial growth conditions[7, 8], the size and shape of the honeycomb lattice arrays [9, 10] and the number of graphene layers and their orientations can all be varied. This structural diversity nourishes hopes for a future carbon-based electronics[11] with band-structure and transport characteristics that can be tailored for different types of applications.

FLG has advantages over single-layer-graphene because it has a larger current-carrying capacity and because its electronic properties are sensitive to more engineerable system parameters[12]. In nature it appears in a variety of stacking arrangements, the most common being Bernal and rhombohedral sequences which can form three dimensional lattices. It has been understood for some time[13] that in graphite θ can depart from Bernal values. With some interesting exceptions[5, 14], most recent studies of inter-layer twists in FLG have focused on samples grown on SiC[15]. In particular Hass *et. al.* have demonstrated that orientational disorder is normally present in carbon-face SiC epitaxial FLG samples[16]. The present work is motivated primarily by the need to achieve a more complete understanding of transport in these graphitic nanostructures, which currently appear to provide the most promising platform for applications.

In a bilayer system, the relative rotation angle θ can be classified as either commensurate or incommensurate[17]. In the former case the misaligned bilayer system still forms a crystal, albeit one with larger lattice vectors and more than four atoms per unit cell. Commensurability occurs at a countably infinite set of orientations; but the probability that a randomly selected orientation angle is commensurate vanishes. The energy bands of commensurate twisted multilayers disperse approximately linearly with momentum [18–20], except at energies very close to the Dirac point. However, the Dirac velocity is reduced

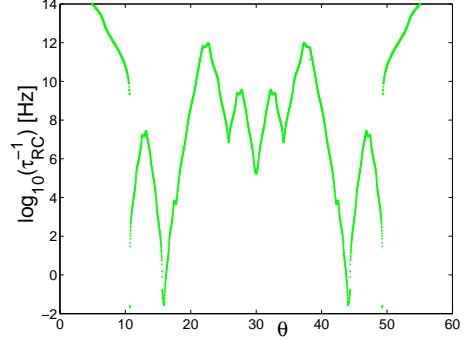


FIG. 1: Interlayer (RC) equilibration rate as a function of twist angle θ . These results were calculated for two layers with equal carrier densities ($n = 5 \times 10^{12} \text{ cm}^{-2}$) and $\epsilon_F \tau = 3$, where ϵ_F is the Fermi energy and τ is the isolated-layer Bloch state lifetime. The relaxation rate is dominated by separate features that appear near every commensurate angle, but differ in strength by many orders of magnitude. The tails of individual features have been cut-off in this plot in order to reveal weaker features that will emerge in more ideal bilayers. Except near $\theta = 0$, the equilibration rate is surprisingly slow for two layers separated by an atomic length scale.

compared to that of a single layer system especially for rotation angles close to 0° or 60° [14, 19]. The linear Dirac-like dispersion contrasts with the approximately quadratic dispersion found in a Bernal stacked bilayer system[21]. Incommensurate bilayers are not crystalline and therefore their electronic properties cannot be analyzed using Bloch's theorem.

Here we develop a theory of the vertical transport properties of twisted FLG samples which is valid in the incoherent transport limit[22]. We show that the specific linear conductance between misaligned layers is enhanced over a small but finite range of twist angles near those that produce relatively short period commensurate structures, that the conductance peak angles shift with in-plane magnetic field B_{\parallel} , and that the peaks become narrower and stronger when the isolated layer Bloch state lifetime τ increases. The differential conductivity tends

to be negative near commensurate conductance peaks and positive otherwise. Typical theoretical results for the dependence of the interlayer equilibration rate on θ are presented in Fig. 1. In the following we first explain the analysis which supports these statements and then discuss some implications for FLG electronics.

Studies of transport between weakly coupled two-dimensional (2D) electron systems have a long history[24, 25] in semiconductor heterojunctions systems. In that case epitaxial tunnel barriers are responsible for nearly perfect 2D momentum conservation, which then helps to make vertical transport a powerful probe of electronic properties. Our theory of vertical transport in FLG is similar to the successful semiconductor heterojunction theory[24]. We derive an expression for tunneling current *I vs.* bias voltage *V* by using a π -orbital tight-binding model, approximating inter-layer hopping processes at leading order in perturbation theory, and accounting for the inevitable presence of a finite disorder potential which limits the life-times of Bloch states in each layer. These steps lead to

$$I(\theta) = eg_s \int \frac{d\omega}{2\pi} [n_{F1}(\omega) - n_{F2}(\omega + eV)] \sum_{\mathbf{k}\mathbf{p}'} |T_{\mathbf{k}\mathbf{p}'}^{\alpha\beta}|^2 A_{1\alpha}(\mathbf{k}, \omega) A_{2\beta}(\mathbf{p}', \omega + eV), \quad (1)$$

where $g_s = 2$ accounts for spin degeneracy, $A_{i\alpha}(\mathbf{k}, \omega)$ is the spectral function for band α and layer i , n_{Fi} is the Fermi distribution function for layer i , and $T_{\mathbf{k}\mathbf{p}'}^{\alpha\beta}$ is the tunneling matrix element between isolated layer Bloch states with band and crystal momentum labels, $|\mathbf{k}\alpha\rangle$ and $|\mathbf{p}'\beta\rangle$. The sums over \mathbf{k} and \mathbf{p}' may be taken over the unrotated and rotated Brillouin zones respectively. We derive Eq. (1) in section 2 of the Supplementary Information, where we justify its neglect of disorder vertex-corrections. In our calculations, A is approximated by a Lorentzian function with full-width-half-maximum \hbar/τ centered on the band energy $\epsilon_{i\alpha}(\mathbf{k})$. (Hereafter $\hbar = 1$ and length is measured in units of $a_c = 1.42\text{\AA}$, the carbon-carbon distance in graphene.) Eq. (1) is valid in the weak tunneling regime in which T is smaller than lifetime broadening $1/\tau$, allowing coherent tunneling processes to be neglected. This condition is satisfied in typical samples except at rotation angles very close to 0° or 60° .

In a twisted bilayer system the tunneling matrix element depends strongly on the relative orientation of the two graphene sheets. The honeycomb lattice vectors of the rotated layer \mathbf{R}' are related to those of the unrotated layer \mathbf{R} by $\mathbf{R}' = M(\theta)\mathbf{R} + \mathbf{d}$. Here M is the transformation matrix for rotations in the lattice plane and \mathbf{d} is a translation vector. Corresponding rotations occur in reciprocal space so that $\epsilon_{1\alpha}(\mathbf{p}) = \epsilon_{2\alpha}(\mathbf{p}')$ when $\mathbf{p}' = M(\theta)\mathbf{p}$. Commensurability is determined only by M , but linear translations of one layer relative to the other do modify T , and hence the tunneling current.

The magnitude of T depends on the π -orbital interlayer hopping amplitudes of our tight-binding model which we

estimate using a simple two center approximation scheme explained in section 1 of the Supplementary Information. We find that

$$T_{\mathbf{k}\mathbf{p}'}^{\alpha\beta} = \frac{1}{\Omega_0} \sum_{s, \bar{s}} (a_{\mathbf{k}s}^{(\alpha)})^* a_{\mathbf{p}\bar{s}}^{(\beta)} \sum_{\mathbf{G}_1 \mathbf{G}_2} t_{\mathbf{k}+\mathbf{G}_1} e^{-i(\mathbf{k}+\mathbf{G}_1)\cdot\mathbf{d}} \times e^{i\mathbf{G}_1\cdot\tau_s} e^{-i\mathbf{G}_2\cdot\tau_{\bar{s}}} \delta_{\mathbf{k}+\mathbf{G}_1, \mathbf{p}'+\mathbf{G}_2} \quad (2)$$

where Ω_0 is the area of a unit cell. Here \mathbf{G}_1 and \mathbf{G}_2 are summed over reciprocal lattice vectors, primed wavevectors are rotated, s and \bar{s} label the two triangular honeycomb sublattices centered at positions τ_s , and $a_{\mathbf{k}s}^{(\alpha)}$ is the sublattice projection of the $|\mathbf{k}\alpha\rangle$ Bloch state in the unrotated layer. In Eq.(2), which is derived in section 1 of the Supplementary Information, $t_{\mathbf{k}}$ is the 2D Fourier transform of the finite-range inter-layer hopping amplitude. As we will explain, the interlayer conductance and the layer equilibration rate are proportional to $|t_{\mathbf{k}}|^2$ values for $|\mathbf{k}|$'s that are larger than the Brillouin-zone scale (except for $\theta \approx 0^\circ, 60^\circ$). Because the inter-layer distance is already larger than the carbon-carbon distance within a layer, these $|t_{\mathbf{k}}|^2$ values tend to be both extremely small and extraordinarily sensitive to details of the inter-layer tunneling model that are otherwise inconsequential.

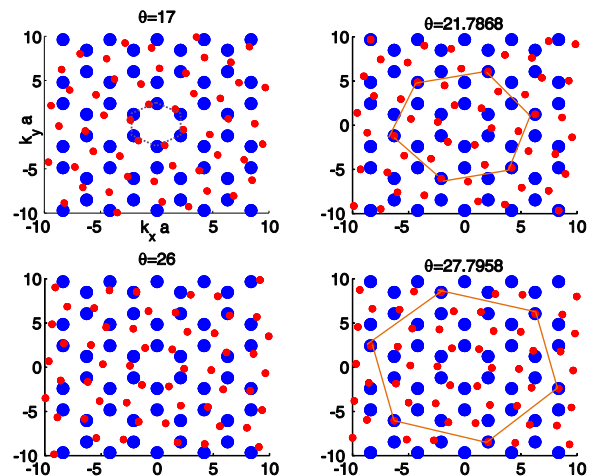


FIG. 2: Fermi circles in an extended zone scheme. The blue(large) and red(small) circles correspond to the Fermi circles in the unrotated and rotated layers respectively. The area enclosed by the circles is proportional to the carrier density. Conductance contributions occur when the Fermi circles intersect and are much larger when the intersection occurs closer to the origin of momentum space. The Brillouin-zone boundary connects the centers of the inner shell of blue circles as indicated by the dashed lines in the $\theta = 17^\circ$ panel.

We have used Eqs.(1) and (2) to evaluate interlayer currents as a function of rotation angle θ , carrier density, bias voltage, and disorder strength. Since for typical electronic densities the temperature T is much less than the Fermi temperature we focus on $T = 0$ hereafter. It is

helpful to first focus on the linear conductance

$$G(\theta) = \frac{e^2 g_s}{2\pi} \sum_{\mathbf{k}\mathbf{p}'} |T_{\mathbf{k}\mathbf{p}'}^{\alpha\beta}|^2 A_{1\alpha}(\mathbf{k}, \epsilon_F) A_{2\beta}(\mathbf{p}', \epsilon_F). \quad (3)$$

The equilibration rate plotted in Fig.1 was obtained by viewing the bilayer as a leaky capacitor and ignoring any screening by graphene σ orbitals. This model yields an RC circuit with time constant τ_{RC} related to the conductance by $G/\mathcal{A} = 0.027 \tau_{\text{RC}}^{-1}$ where \mathcal{A} is the layer area in m^2 , G is measured in Siemens, and τ_{RC} in seconds. Apart from a change in scale, Fig.1 can then be viewed as a plot of the interlayer conductance. We find that the tunneling conductance increases abruptly near commensurate angles, that the height of the peaks scales linearly with $\epsilon_F \tau$ (for $\epsilon_F \tau > 1$), and that the peaks narrow as τ increases. The discontinuous jumps of $\log(G)$ in Fig.1 are artificial and result from a numerical procedure in which momenta \mathbf{k} and \mathbf{p}' in Eq.(3) are restricted to the vicinity of the Fermi energy. This procedure suppresses the tails of all commensurate features, allowing more minor features to be revealed. In practice the conduction tails corresponding to highly commensurate structures will dominate G over a range of angles that depends on τ . Limited by computational power we considered $\tau^{-1} \approx 75 \text{ meV}$ in Fig.1 however in epitaxial graphene the lifetime can be more than an order of magnitude longer[26]. An accurate theory of the conduction-peak tails would require a reliable theory of the isolated-layer spectral function tails.

Why is the tunneling conductance enhanced at commensurate rotation angles? To understand the relation between interlayer current and commensurability it is illuminating to plot the Fermi surfaces of both layers, periodically extended in momentum space by adding reciprocal lattice vectors to the crystal momenta of the electrons. As we see in Eq.(2), allowed interlayer tunneling processes are diagonal in this generalized momentum. The left panels in Fig.2 corresponds to the incommensurate rotation angles $\theta = 17^\circ, 26^\circ$ whereas the right panels correspond to the commensurate angles near $\theta = 21.8^\circ, 27.8^\circ$. We use different Fermi surfaces sizes for clarity; similar considerations apply independent of the sign or magnitude of the carrier density ratio. The key feature to notice in these plots is that at commensurate rotation angles some Fermi spheres overlap. Overlaps of circles centered on the extended Dirac points, *always* accompany commensurate real-space structures because the set of extended Dirac points forms a momentum space honeycomb lattice that differs from the real space honeycomb lattice only by a scale factor and by a rotation. If overlaps occur in real-space, they also occur in momentum space. Notice that this property holds only when the Brillouin-zone corners are extended to fill momentum space; if the Dirac point occurred elsewhere in the isolated layer Brillouin-zone, the dependence of inter-layer conductance on θ would be quite different.

The overlap of extended Dirac points does not fully explain the conductance peaks at finite density, since Fermi

energy states at finite carrier density are displaced from the Dirac point. The nesting between Fermi surfaces alluded to in Fig.2 actually depends not only on commensurability, but also on the fact that for typical carrier densities the Fermi surface is well approximated by a circle centered on the Brillouin-zone corners. For equal densities then, matching Dirac points implies complete Fermi surface nesting (see Fig.3). When the two-layers have different densities, the peak conductance will not occur at the nesting angle; instead the conductance will have a double-peak structure with features offset to both sides of the commensurate angle.

Commensurate rotation angles can be classified as either inter-valley or intra-valley. In the former the two Dirac points k_D and k'_D that coincide in the extended momentum picture are associated with different valleys (in the aligned bilayer) whereas for intra-valley rotation angles they belong to the same valley. An inter-valley commensurate rotation is illustrated in Fig.3.

Away from commensurate angles the energy difference between states which have the same extended momentum is typically much larger than the Fermi energy, and the spectral function width $1/\tau$ (see left panels of Fig.2). The conductance is therefore very small away from the commensurate-angle peaks. The Dirac-like linear spectrum of an ideal commensurately twisted bilayer does not, as is commonly stated, indicate that the ideal twisted layers are decoupled. At commensurate angles the perfect crystal wavefunctions near the Dirac point are in fact coherent equal weight contributions from the two layers. In the limit of large in-plane Bloch state lifetimes, the conductance becomes very large and eventually the incoherent transport picture will fail.

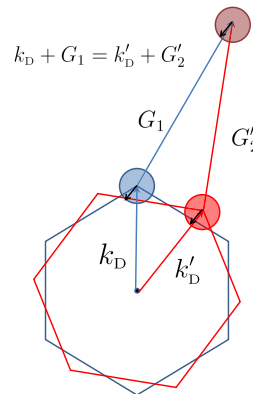


FIG. 3: Nesting of Dirac cones at commensurability. For commensurate rotation angles every momenta state on the rotated Fermi circle is mapped onto a momenta state of an unrotated Fermi circle.

As we have explained, vertical transport at commensurability is dominated by processes in which an electron tunnels from a momentum near a Dirac point of one layer, to a momentum that is the same distance from a Dirac point of the other layer. Since carrier densities per unit cell are always small, we can replace $t_{\mathbf{k}+\mathbf{G}}$ in Eq.(2) by

$t_{\mathbf{k}_D+\mathbf{G}}$ where \mathbf{k}_D is the Dirac point momentum. We then find that the conductance peak can be expressed as the product of geometry-related and phase space factors:

$$G \approx R(\theta_c, \mathbf{d}) \sum_{\mathbf{k}} A_1(\mathbf{k}, \epsilon_F) A_1(\mathbf{k}, \epsilon_F), \quad (4)$$

where θ_c is the commensurate orientation. $R(\theta_c, \mathbf{d})$ depends mainly on the value of $t_{|\mathbf{k}_D+\mathbf{G}|}$ at which the extended Dirac points overlap (see Fig.2), while the remaining phase space factor is identical to the one that appears in the theory of coupled quantum wells[24]. For equal densities in the two layers, the Fermi surfaces nest precisely. For pure rotations R can be calculated analytically. For inter-valley commensurate rotation angles we find that

$$G(\theta_c) = A_{g_s} g_v \frac{e^2 \epsilon_F \tau E_g^2(\theta_c)}{\hbar 16\pi v^2}. \quad (5)$$

Here E_g is the energy difference between the top conduction band and bottom valence band of the twisted bilayer at the Dirac point, and we assumed that $\epsilon_F \tau > 1$. In section 4 of the Supplementary Information we derive Eq.(30) and obtain a similar formula for intra-valley rotation angles. In addition we numerically verify that the conductance changes only by a factor of order unity as \mathbf{d} is varied across the unit cell. Eq.(30) therefore provides a good estimate for G regardless of the relative translation between the two layers (see section 3 of the Supplementary Information).

When the densities differ, Fermi circles in different layers begin to overlap near $\theta = \theta_c$ only after a momentum-space relative shift \mathbf{Q} equal in magnitude to the difference of the two Fermi wavevectors. As in semiconductor double-wells[24, 25, 27], a shift $\mathbf{Q} = \hat{\mathbf{z}} \times \hat{\mathbf{e}}_d l_H^2$, where l_H is the magnetic length, can be accomplished in a bilayer with layer separation d_\perp by applying an in-plane magnetic field $B_\parallel \hat{\mathbf{e}}$. For graphene bilayers, however, a relative momentum space shift can also be achieved by rotation, as is clear from Fig.2. For small departures from commensurability $\mathbf{Q} \approx (\theta - \theta_c) \hat{\mathbf{z}} \times (\mathbf{k}_D + \mathbf{G})$. For equal densities, both rotations and in-plane fields dramatically suppress the conductance peak when $vQ \geq 1/\tau$ where v is the band velocity of graphene. For example, for $n = 4 \cdot 10^{12} \text{cm}^{-2}$ and $\tau = 50 \text{fsec}$ [31], the conductance peak should nearly completely disappear at 0.15 Tesla. FLG should therefore provide a palette on which gate voltages, in-plane magnetic fields, and rotations can be mixed to produce a rainbow of interrelated and extraordinarily strong magnetic-field and strain sensitive resistance effects.

In general the interlayer conductance $G(\theta)$ is peaked whenever any extended Fermi surface overlap occurs at reasonably small reciprocal lattice vectors. The degree of overlap can be parameterized by q^* , the minimum separation between extended Dirac points of the rotated and unrotated layers for a reciprocal lattice vector truncation chosen to reflect the scale on which t_q falls off. For a clean

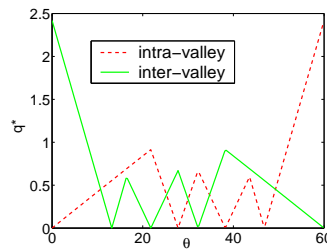


FIG. 4: The minimum separation between extended Dirac points q^* as a function of rotation angle θ .

system, tunneling conductance at equal density is appreciable as long as $q^* \approx |\theta - \theta_c| |\mathbf{k} + \mathbf{G}| < 2k_F$. Because $2k_F$ in FLG electronic systems is always small compared to reciprocal lattice vector scales, the conductance peaks are invariably sharp when plotted as a function of θ . As an example $q^* \approx 6.39|\theta - \theta_c|$ in the vicinity of $\theta_c = 27.8^\circ$ for the reciprocal lattice vector illustrated in Fig.2. In Fig.4, q^* , minimized over the first two G-shells, is plotted as a function of angle. Overlap between the Fermi spheres of the two layers will therefore persist over the angle range for which q^* is smaller than $2k_F$.

Electronic structure calculations for ideal commensurate bilayers demonstrate that E_g decreases very rapidly as the number of atoms per unit cell increases[17]. $E_g = 780 \text{meV}$ for a unit cell of 4 atoms, and already less than 1 meV for a unit cell of 100 atoms. It is therefore plausible that conductance tails that correspond to the few most lowest order commensurate angles (e.g. $\theta_c = 0^\circ, 21.8^\circ, 27.8^\circ, 32.2^\circ, 38.2^\circ, 60^\circ$) will dominate G at every rotation angle. Eqs.(4) and (30) should therefore be interpreted as a lower bound for the conductance at higher order commensurate θ_c 's.

We now turn to the non-linear $I - V$ of twisted bilayer graphene. At zero temperature

$$I(\theta, V) = \frac{eg_s}{2\pi} \sum_{kp} |T_{kp'}|^2 \int_{\epsilon_F - eV}^{\epsilon_F} d\omega A_1(k, \omega) A_2(p', \omega + eV). \quad (6)$$

We numerically find that the I-V curves at commensurate and incommensurate angles are drastically different. At relatively small bias voltage the currents corresponding to commensurate angles are several orders of magnitude larger than their incommensurate counterparts. On the other hand negative differential conductances invariably appear at commensurate angles, whereas dI/dV tends to be small and positive at incommensurate angles.

In classic tunneling experiments, a bias voltage induces an equal electric potential difference between the layers. Total energy conservation then implies kinetic energy changes equal to eV upon tunneling. Since, as we have explained, the allowed tunneling processes at commensurate angles are between states with the same kinetic energy bias voltages tend to decrease tunneling currents. Following the same approximations that led to Eq.(4) we can capture this effect mathematically by expressing the

interlayer current in product form:

$$I = \frac{e}{2\pi} \sum_{\alpha\beta} R^{\alpha\beta}(\theta, \mathbf{d}) \int_{-\infty}^{\infty} d\omega [n_{\mathbb{F}}(\omega) - n_{\mathbb{F}}(\omega + V)] \times \sum_{\mathbf{K}} A_{\alpha}(k, \omega) A_{\beta}(k, \omega + eV) \quad (7)$$

In Eq.(7) we have allowed for both intraband and interband tunneling at large biases. As long as $eV < \epsilon_{\mathbb{F}}$ tunneling between conduction bands dominate I when both layers are n-type. In this intermediate non-linear regime the two Lorentzian shaped spectral functions in Eq.(7) overlap only weakly and

$$I(\theta_c, \mathbf{d}) \approx G(\theta_c, \mathbf{d}) \frac{V}{1 + (eV\tau)^2}. \quad (8)$$

for $\epsilon_{\mathbb{F}}\tau > 1$. Negative differential conductance occurs when $eV\tau > 1$. For incommensurate twist angles, crystal momenta conservation can not be sustained at the Fermi surface. Increasing V unblocks processes in which tunneling occurs between states with different kinetic energies and leads to a slow increase of the tunneling current with a complex dependence on $t_{\mathbf{q}}$ and \hbar/τ . For $eV > \epsilon_{\mathbb{F}}$, the current increases monotonically with V for both commensurate and incommensurate twist angles. The commensurate tunneling current has a sharp rise at $eV = 2\epsilon_{\mathbb{F}}$ due to momentum conserving processes allowed at high bias voltage in which a valence band electron in one layer tunnels to the conduction band of the opposite layer. For commensurate angles it follows from (7) that these inter-band processes eventually dominate the tunneling current and that

$$I \approx \frac{e^2}{4v^2} R^{vc} \Theta(V - 2\epsilon_{\mathbb{F}}) V \quad (9)$$

to leading order in $1/V\tau$. Here Θ is the Heaviside step function. The finite temperature corrections to Eqs.(8,9) are exponentially small in $T/\epsilon_{\mathbb{F}}$.

The extension of our theory to FLG is straightforward in the linear regime. In the simplest case each layer is rotated with respect to its neighbors sufficiently to drive the system into an incoherent transport regime. The weak links between layers then act like classical resistors which appear in series in vertical transport. The resistance of each link depends on the rotation angle between

layers and on the densities in both layers. We anticipate a very rich and complex behavior of FLG in the non-linear regime. The negative differential conductivities are likely to give rise to steady state multistability and to chaotic temporal response, as occurs in semiconductor multiple-quantum-well systems[32]. A more complicated scenario could arise in turbostratic graphene. There the entire layered structure is composed of a set of coherent multi-layer substructures, characterized by either a Bernal or an AA stacking sequence. Weak links which play a dominant role in limiting vertical conductance appear due to occasional twists. The calculations for the resistance of each twisted interface closely follow those outlined above for the two-layer case when supplemented by a band index for the various 2D energy bands of a coherent substructure.

One application of our theory is to assess whether or not twisted graphene layers are effectively isolated from an electrical point of view. The equilibration time between layers that are spatially uniform but out of equilibrium is plotted in Fig. 1 and is very long compared to characteristic electronic time scales for rotation angles far from important commensurabilities, near 10° for example. The steady-state equilibration length between separately contacted layers can be estimated by equating inter-layer conductances, which are proportional to sample area, with the intra-layer conductance per square. For the commensurate angle $\theta_c = 21.8^\circ$, for example, the sample area at which they are identical is approximately $0.04\mu m^2$. As evident from Fig.1, the corresponding areas for small rotation angles near the AA and AB stacking sequences are even smaller. For small rotation angles, the two layers are therefore strongly coupled.

Finally we remark that the extraordinary sensitivity of the tunneling conductance to the twist angle found here suggests that misaligned graphene bilayers might be useful as ultra-sensitive strain gauges or pressure sensors[33] which are widely used in biological, mechanical and optical systems.

The authors acknowledge support from CERA, SWAN and the Welch Foundation and helpful conversations with W. de Heer, R. Duine, P. First, D. Goldhaber-Gordon, R. Lifshitz, and E. Tutuc.

Supplementary Information

I. THE TUNNELING MATRIX ELEMENTS

The interlayer hopping terms in a π -band tight-binding Hamiltonian for twisted graphene bilayers depend in general on the positions of all carbon atoms. Our analysis of inter-layer conductance and equilibration is based on a simple two-center model in which the interlayer hopping parameter between two sites, $t(\mathbf{r})$, depends only on the planar

projection of their separation \mathbf{r} . In the main text we used an equation, derived below, which relates the inter-layer hopping amplitudes of twisted bilayers to $t_{\mathbf{q}}$, the two-dimensional Fourier transform of $t(\mathbf{r})$.

One strategy which can be used to estimate $t(\mathbf{r})$ is to assume functional forms for the distance dependence of the Slater-Koster $t_{pp\sigma}$ and $t_{pp\pi}$ hopping functions[34], and then fit them to accurately known parameters of untwisted bilayers. We have explored this approach, following the procedures adopted in Refs. [17, 28], but have concluded that it tends to underestimate hopping amplitudes near the Dirac points of twisted bilayers. We have therefore decided to obtain numerical estimates by directly fitting an *ansatz* for $t_{\mathbf{q}}$ to obtain

$$t_{\mathbf{q}} = t_0 e^{-\alpha(qd_{\perp})^{\gamma}}, \quad (10)$$

where $t_0 = 2 eV\text{\AA}^2$, $\alpha = 0.13$, $\gamma = 1.25$, and $d_{\perp} = 3.34\text{\AA}$ is the distance between the layers. The value used for t_0 is the average of values implied by the models in Refs.[17, 28]. Since t_0 is the sum of all inter-layer hopping parameters, it should be estimated reliably by any parameterization that uses accurate values for the largest hopping parameters. We fix α and γ so that the values of the ideal bilayer gaps are accurate for the lowest order commensurate structures. These are proportional to t_{k_D} ($\theta = 0^\circ$ and $\theta = 60^\circ$) and $t_{6.4/a_c}$ ($\theta = 21.8^\circ$ and $\theta = 38.2^\circ$) where $a_c = 1.42\text{\AA}$ is the carbon-carbon distance in single layer graphene. See details in Sec. IV below. We fit the energy gaps to values extracted from the *ab initio* calculations by Shallcross *et al.*[17]. Note that these values of $t_{\mathbf{q}}$ characterize short-distance roughness in the inter-layer hopping landscape which survives Fourier transformation at large wavevectors, which is not simply related to typical inter-layer hopping strengths. The energy gaps that we obtain at $\theta = 21.8^\circ$ using the real space parameterizations of $t_{pp\sigma}(r)$ and $t_{pp\pi}(r)$ in Refs. [17, 28] are both substantially smaller than the *ab initio* gaps of Shallcross *et al.*[17].

We now derive the expression for the hopping amplitude between Bloch states in twisted bilayers that is used in the main text. The Bloch state in layer j with crystal momentum \mathbf{k} and band index α can be written as

$$|\Psi_{\mathbf{k}\alpha}^{(j)}\rangle = a_{\mathbf{k}A}^{j\alpha} |\psi_{\mathbf{k}A}^{(j)}\rangle + a_{\mathbf{k}B}^{j\alpha} |\psi_{\mathbf{k}B}^{(j)}\rangle \quad (11)$$

where A and B label the two triangular honeycomb sublattices,

$$\begin{pmatrix} a_{\mathbf{k}A}^{1\alpha} \\ a_{\mathbf{k}B}^{1\alpha} \end{pmatrix} = \frac{1}{\sqrt{2}} \begin{pmatrix} e^{i\Theta_{\mathbf{k}}} \\ \alpha \end{pmatrix}, \quad (12)$$

and $\Theta_{\mathbf{k}}$ is the phase of the inter-sublattice hopping term in the single-layer tight-binding model. For nearest neighbor hopping within the planes $\Theta_{\mathbf{k}} = \arg\left(\sum_j e^{i\mathbf{k}\cdot\delta_j}\right)$ where the δ_j are the three vectors connecting an atom with its nearest neighbors. The Bloch state projection on sublattice s is

$$|\psi_{\mathbf{k}s}^{(1)}\rangle = \frac{1}{\sqrt{N}} \sum_{\mathbf{R}} e^{i\mathbf{k}(\mathbf{R}+\tau_s)} |\tau_s + \mathbf{R}\rangle, \quad (13)$$

where $|\tau_s + \mathbf{R}\rangle$ is a site-representation basis function of the tight-binding model. In Eq.(13) \mathbf{R} is a triangular lattice vector, N is the number of unit cells in the system, and we choose $\tau_A = 0$ and τ_B equal to the vector connecting the two atoms within a unit cell.

The relative orientation of the two layers can be described by a rotation matrix $M(\theta)$ and a translation vector \mathbf{d} . Therefore every Bloch wave function in the second layer is related to a Bloch wave function in the first layer by

$$|\Psi_{\mathbf{k}'\alpha}^{(2)}\rangle = |\Psi_{\mathbf{k}\alpha}^{(1)}\rangle \quad (14)$$

with $|\mathbf{R} + \tau_s\rangle$ in layer 1 replaced by $|\mathbf{R}' + \tau'_s\rangle$ in layer 2, $\mathbf{r}' = M\mathbf{r} + \mathbf{d}$ for all positions and $\mathbf{k}' = M\mathbf{k}$. Using primes to indicate layer 2 variables and invoking the two-center approximation for the inter-layer tunneling amplitude,

$$\langle \tau_s + \mathbf{R} | H_{inter} | \tau'_s + \mathbf{R}' \rangle = t(\tau_s + \mathbf{R} - \tau'_s - \mathbf{R}'), \quad (15)$$

we find that

$$\langle \Psi_{\mathbf{k}\alpha} | H_{inter} | \Psi_{\mathbf{p}'\beta} \rangle \equiv T_{\mathbf{k}\mathbf{p}'}^{\alpha\beta} = \frac{1}{N} \sum_{ss'} \left(a_{\mathbf{k}s}^{(\alpha)} \right)^* a_{\mathbf{p}s'}^{(\beta)} \sum_{\mathbf{R}_1\mathbf{R}_2} e^{-i\mathbf{k}\cdot(\mathbf{R}_1+\tau_s)+i\mathbf{p}\cdot(\mathbf{R}_2-\mathbf{d}+\tau'_{s'})} t(\mathbf{R}_1 + \tau_s - \mathbf{R}'_2 - \tau'_{s'}).$$

Expression (2) in the main text is obtained by Fourier expanding $t(\mathbf{r})$ and summing over the lattice vectors.

II. VERTEX CORRECTIONS

The general expression for the tunneling current

$$I(\theta, V) = -4eg_s \int \frac{d\omega}{2\pi} \sum T_{\mathbf{k}_0\mathbf{p}'_0}^{\alpha\beta} T_{\mathbf{k}_N\mathbf{p}'_N}^{\gamma\delta*} [n_2(\omega + eV) - n_1(\omega)] \times \overline{ImG_{1\gamma\alpha}^R(\mathbf{k}_N, \mathbf{k}_0, \omega) ImG_{2\beta\delta}^R(\mathbf{p}'_0, \mathbf{p}'_N, \omega + eV)} \quad (16)$$

is obtained using second order perturbation theory[35]. In Eq.(16) n_j is the Fermi distribution in layer j , $G_{j\gamma\alpha}^R$ is the retarded Green function in layer j that correspond to the propagation of a charge carrier from band α to band γ , the rotation angle is θ , and V is the bias voltage. The over-line denotes disorder averaging. As in the main text, primed variables are associated with the rotated layer. Since disorder breaks translation invariance, the Green functions are not diagonal in the momentum representation. When the disorder averages can be performed independently for the two-layers, translational invariance is recovered and Eq. (16) reduces to Eq.(1) of the main text.

We average over disorder using the self-consistent Born approximation in which correlations between the layers appear as a vertex-correction ladder diagram sum (see Fig.5). For simplicity we assume white noise disorder and characterize the correlation between the disorder potentials in the two layers by $\gamma = n_i \langle U_1 U_2 \rangle$ where n_i is the concentration of impurities and U_j is the disorder potential in layer j . For aligned bilayers with short range tunneling we find that

$$G = \frac{e^2 t^2 \nu_F \tau}{2} \frac{1}{1 - \gamma/\beta} \quad (17)$$

where $\beta = n_i \langle U_j^2 \rangle$. As evident from Eq.(17) the tunneling conductance diverges if the disorder potentials of the two layers are perfectly correlated. These strong correlations are likely in a graphene bilayer because of the small distance between the layers. The divergence of G indicates the breakdown of perturbation theory, *i.e.* it invalidates the incoherent theory we use in this work. A similar scenario arises for tunneling between coupled semiconductor quantum wells[23] when their disorder potentials are strongly correlated.

We now show that vertex corrections are important only at very small values of the rotation angle θ . The physical origin of this behavior is twofold. First, the relevant correlation in the twisted case is between the disorder potential in one layer and a spatially rotated counterpart in the other layer. For any finite range disorder correlation length, these two disorder potentials are independent making γ in Eq.(17) considerably smaller. Second, the divergence in the conductance appears due to tunneling between identical states. However, for incommensurate angles the wave vectors of the initial and final states in a tunneling process substantially differ making β in Eq.(17) considerably larger. In the following paragraphs we explain how this latter behavior is captured in a diagrammatic perturbation theory description of a disordered system.

We first focus on the tunneling conductance for aligned layers ($\theta = 0$). At zero temperature

$$G(\theta) = \frac{2e^2 g_s}{\pi} \sum T_{\mathbf{k}_0\mathbf{p}'_0}^{\alpha\beta} T_{\mathbf{k}_N\mathbf{p}'_N}^{\gamma\delta*} \overline{ImG_{1\gamma\alpha}^R(\mathbf{k}_N, \mathbf{k}_0, \epsilon_F) ImG_{2\beta\delta}^R(\mathbf{p}'_0, \mathbf{p}'_N, \epsilon_F)}. \quad (18)$$

The conservation of crystal momentum in expression (2) for $T_{\mathbf{k}\mathbf{p}'}^{\alpha\beta}$ implies that $\mathbf{p}_0 = \mathbf{k}_0$ and that $\mathbf{p}_N = \mathbf{k}_N$. For

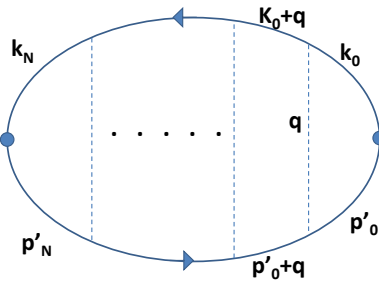


FIG. 5: Self consistent Born approximation. A bubble diagram with ladders.

$\epsilon_F \tau > 1$ interband transitions are inhibited so that $\alpha = \gamma$ and $\beta = \delta$. Due to the spinor form of the wave functions each disorder line contributes $[1 + \cos(\theta_{k_{j+1}} - \theta_{k_j})]\gamma/2$ to the ladder diagram. To evaluate $\Pi^{(n)}$, the ladder diagram

with n disorder lines, we first integrate over the angular variables using

$$\int_0^{2\pi} \frac{d\theta_q}{2\pi} \cos(\theta_{k_1} - \theta_q) \cos(\theta_{k_2} - \theta_q) = \frac{1}{2} \cos(\theta_{k_1} - \theta_{k_2}). \quad (19)$$

Then using $\mathcal{F}(0) = 2\pi\nu_F\tau$ where

$$\mathcal{F}(\mathbf{Q}) = \sum_q G_{1\alpha}^R(q, \omega) G_{1\alpha}^A(\mathbf{q} + \mathbf{Q}, \omega) \quad (20)$$

we integrate over the radial direction. In obtaining $\mathcal{F}(0)$ we have replaced the energy dependent density of states by ν_F , its value at the Fermi energy. We find that for $n \geq 1$

$$\Pi^{(n)} = G_1^\mu(k_0) G_2^\nu(k_0) \left[1 + \frac{1}{2^{n-1}} \cos(\theta_{k_0} - \theta_{k_N}) \right] \left(\frac{\gamma}{\beta} \right)^{n-1} \frac{\gamma}{2} G_1^\mu(k_N) G_2^\nu(k_N) \quad (21)$$

where $\beta = 1/\pi\nu_F\tau$ and $\mu, \nu = R, A$. For $n \geq 2$ the Green functions in one layer are retarded and those of the other layer are advanced. We now sum $\Pi^{(n)}$ to infinite order in n . While the sum can clearly be carried for a general tunneling matrix element T_{kk} the basic physical idea is more transparent for short range tunneling. Therefore in the calculations below we assume $T_{kk} = t$ is momentum independent in which case we recover Eq.(17).

We now address the role played by vertex corrections in twisted bilayers. As in the main text our discussion excludes the vicinity of $\theta = 0^\circ, 60^\circ$ for which $t > 1/\tau$. The procedure outlined above for calculating G can be repeated for any rotation angle θ . For a rotated bilayer it follows from Eq.(2) in the main text that $\mathbf{k}_0 - \mathbf{p}'_0 = \mathbf{G}'_2 - \mathbf{G}_1 \equiv \mathbf{Q}$ where $Q \approx |\mathbf{k}_D + \mathbf{G}_1| |\theta - \theta_c|$. Expression (17) can then be used for a rotated bilayer as well if β is replaced by

$$\beta_Q = \beta F(0)/F(Q). \quad (22)$$

Because \mathcal{F} is a monotonically decreasing function of its argument and because Q is comparable in size to the Dirac momentum $\beta_Q \gg \beta$.

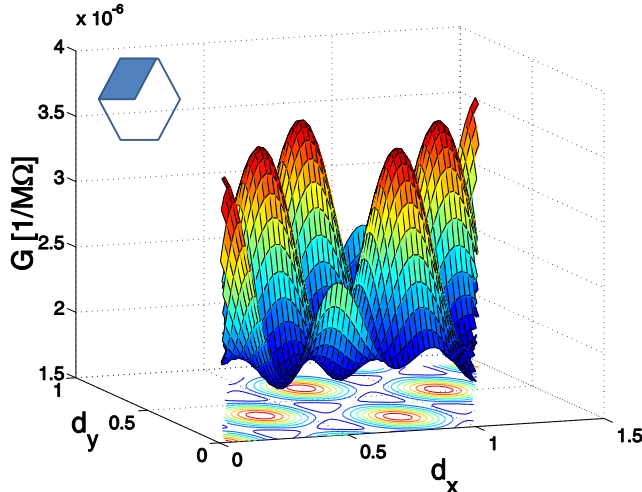


FIG. 6: Dependence of conductance per unit cell G on translation \mathbf{d} for $\theta = 27.8^\circ$, $\epsilon_F\tau = 3$, and $n = 5 \cdot 10^{12} \text{ cm}^{-2}$.

III. DEPENDENCE OF TUNNELING CURRENT ON TRANSLATION

Commensurability depends only on the relative rotation of the two graphene layers. Nevertheless linear translation of one layer with respect to the other will change the tunneling current. In Fig.6 the conductance at $\theta = 27.8^\circ$ is plotted as a function of \mathbf{d} for a bilayer with $n = 5 \cdot 10^{12} \text{ cm}^{-2}$ in each layer and $\epsilon_F\tau = 3$. The dependence of the tunneling current on \mathbf{d} is captured by the phase factor $\exp[-i(\mathbf{k} + \mathbf{G}_1) \cdot \mathbf{d}] \simeq \exp[-i(\mathbf{k}_D + \mathbf{G}_1) \cdot \mathbf{d}]$ in the tunneling matrix element $T_{\mathbf{k}\mathbf{p}'}$. When summed over \mathbf{k} the result is a rapid spatial variation on the lattice constant scale,

illustrated in Fig.6 due to the $\exp[-i(\mathbf{k}_D + \mathbf{G}_1) \cdot \mathbf{d}]$ factor, modulated by a slower variation on the Fermi wavelength scale.

As illustrated in Fig.1 the conductance peaks appear symmetrically around $\theta = 30^\circ$, but the height of a peak with $\theta < 30^\circ$ does not necessarily equal the height of the corresponding peak at $\theta' = 60^\circ - \theta$. In fact, the relative height of the two peaks depends on \mathbf{d} . An AA stacking sequence can be transformed to Bernal stacking either by a pure rotation with $\theta = 60^\circ$ or by a translation with $\mathbf{d} = (1, 0)$. Since the latter transformation does not influence commensurability any commensurate angle θ_c of the AA stacked bilayer is a commensurate angle of the Bernal stacked bilayer. The conductance peaks then lie symmetrically with respect to $\theta = 30^\circ$ since if θ is commensurate so is its inverse.

IV. CONDUCTANCE FOR COMMENSURATE ANGLES FOR $\mathbf{d} = 0$.

For commensurate angles the conductance can be approximated by Eq.(4) in the main text. The integration over the overlap of the two spectral functions

$$\sum_{\mathbf{k}} A_1(k, \epsilon_F) A_1(k, \epsilon_F) = \frac{A}{2\pi v^2} [2 + 2\pi\epsilon_F\tau + 4\epsilon_F\tau \arctan(2\epsilon_F\tau)] \quad (23)$$

is independent of the rotation angle and the entire dependence of G on the relative alignment of the two layers is in $R_{\mu\nu}(\theta, \mathbf{d})$. We now evaluate R for $\mathbf{d} = 0$.

At the Dirac point the intra-layer Hamiltonian vanishes and we have contributions only from interlayer tunneling:

$$H_0 = \begin{pmatrix} 0 & \mathcal{T} \\ \mathcal{T}^\dagger & 0 \end{pmatrix} \quad (24)$$

where each element is a 2×2 block for the two π -bands in each layer. Using a representation of sublattice sites in each layer we find that

$$\mathcal{T} = \mathcal{T}^S = \begin{pmatrix} 2|a| & 0 \\ 0 & 2|a| \cdot e^{-2i\phi} \end{pmatrix}, \quad \mathcal{T} = \mathcal{T}^D = \begin{pmatrix} 2|a| & 0 \\ 0 & 0 \end{pmatrix}. \quad (25)$$

Here \mathcal{T}^S and \mathcal{T}^D correspond respectively to intra-valley (S=same) and inter-valley (D=different) rotation angles as explained in the main text, and $\phi = 0, \pm 60$ depends on θ_c : *e.g.* $\phi(0^\circ) = 0$, $\phi(27.8^\circ) = 60^\circ$ and $\phi(38.2^\circ) = -60^\circ$. If the hopping amplitude t_q decreases fast enough with momentum so that only the first G -shell significantly contribute to the tunneling matrix

$$|a| = 1.5 \frac{t_{\mathbf{k}_D + \mathbf{G}_1}}{\Omega_0} \quad (26)$$

where Ω_0 is the area of a unit cell and \mathbf{G}_1 is the wavevector which produces the smallest \mathbf{q} extended-zone Dirac-cone overlap as explained in the text. In our model Eq.(26) is satisfied for all commensurate angles except for $\theta = 0^\circ, 60^\circ$ for which $|a| = 1.67t_{\mathbf{k}_D + \mathbf{G}_1}/\Omega_0$. Diagonalizing H_0 yields $E^S = \pm 2|a|$ (both doubly degenerate) and $E^D = 0, 0, \pm 2|a|$. In both cases the energy gap between the top conduction band and bottom valence band is therefore $E_g = 4|a|$.

To find R we assume that T is well approximated by Eq.(25) for finite momentum states in the vicinity of the Dirac points. We verified this assumption numerically for low densities. We first focus on inter-valley rotation angles. In the eigenstate representation

$$T_{kp'}^{\mu\nu} = a_{k\mu}^{1\alpha*} a_{k\nu}^{1\beta} \mathcal{T}_{kp'}^{\alpha\beta} \delta_{kp'}. \quad (27)$$

It follows from Eqs.(25,27) that

$$T^D = e^{i(2\theta_k + \theta_c)} |a| I. \quad (28)$$

Consequently,

$$R_{\mu\nu}^D = \int \frac{d\theta_k}{2\pi} |T^{\mu\nu}(\theta_k)|^2 = |a| I \quad (29)$$

and

$$G^D(\theta_c, d=0) = \mathcal{A} g_v g_s \frac{e^2 E_g^2(\theta_c)}{\hbar 64\pi^2 v^2} [2 + 2\pi\epsilon_F\tau + 4\epsilon_F\tau \arctan(2\epsilon_F\tau)]. \quad (30)$$

Expression (5) is obtained in the $\epsilon_F \tau > 1$ limit.

Similarly for intra-valley rotation angles

$$T^S = 2e^{i(\phi + \frac{\theta_c}{2})} |a| \begin{pmatrix} \cos(\phi - \frac{\theta_c}{2}) & -i \sin(\phi - \frac{\theta_c}{2}) \\ -i \sin(\phi - \frac{\theta_c}{2}) & \cos(\phi - \frac{\theta_c}{2}) \end{pmatrix} \quad (31)$$

It then follows that

$$R_{\mu\nu}^S = \frac{E_g^2}{4} \begin{pmatrix} \cos^2(\phi - \frac{\theta_c}{2}) & \sin^2(\phi - \frac{\theta_c}{2}) \\ \sin^2(\phi - \frac{\theta_c}{2}) & \cos^2(\phi - \frac{\theta_c}{2}) \end{pmatrix} \quad (32)$$

and that the conductance is

$$G^S(\theta_c, d=0) = \mathcal{A} g_v g_s \frac{e^2}{\hbar} \frac{E_g^2(\theta_c)}{16\pi^2 v^2} \cos^2\left(\phi - \frac{\theta_c}{2}\right) [2 + 2\pi\epsilon_F \tau + 4\epsilon_F \tau \arctan(2\epsilon_F \tau)]. \quad (33)$$

Note that inter-band resonant conduction (which occurs when the carrier densities in the two layers are opposite) has the same form as its intra-band counterpart for inter-valley rotation angles. For the inter-band conduction at inter-valley rotation angles the cos function in Eq.(33) should be replaced by a sin. Interestingly, the ratio

$$\Delta G(\theta_c) \equiv \frac{G^S(\theta_c, d=0)}{G^D(60^\circ - \theta_c, d=0)} = 4 \cos^2\left(\phi - \frac{\theta_c}{2}\right) \quad (34)$$

depends only on the twist angle. For example, $\Delta G(27.8^\circ) = 1.94$ in accord with the numerical results depicted in Fig.6.

Using the momentum dependent T matrices we can find the bands in the vicinity of the Dirac points. For inter-valley rotations we find four non-degenerate bands

$$E_k^D = \pm \sqrt{\epsilon_k^2 + 2|a|^2 \pm 2\sqrt{\epsilon_k^2 |a|^2 + |a|^4}}. \quad (35)$$

At low energies $\epsilon_k \ll a$

$$E_{k1}^D = \pm \frac{k^2}{2m^*}, \quad E_{k2}^D = \pm 2|a| \pm \frac{k^2}{2m^*} \quad (36)$$

where $m^* = |a|/v^2$. For the intra-layer rotations

$$E_k^S = \pm \sqrt{\epsilon_k^2 + 4|a|^2 \pm 4|a|\epsilon_k \cos(\phi - \theta_c/2)} \quad (37)$$

At low energies $\epsilon_k \ll a$

$$E_k^S = \pm 2|a| \pm v^* k \quad (38)$$

where $v^* = v \cos(\phi - \theta_c/2)$. Deviations from expressions (25) for \mathcal{T} result in trigonal warping in a bilayer system. More elaborate studies of the spectrum are needed to determine whether such effects are important in a rotated bilayer system as well.

-
- [1] Castro Neto, A. H. *et al.* The electronic properties of graphene. *Rev. Mod. Phys.* **81**, 109 (2009)
 [2] Geim, A.K., & MacDonald, A.H. Graphene: Exploring carbon flatland. *Physics Today* **60**, 35-41 (2007).
 [3] Chen, J. H., Jang, C., Xiao, S., Ishigami, M., & Fuhrer M. S. Intrinsic and extrinsic performance limits of graphene devices on SiO₂. *Nature Nanotech.* **7**, 206-209

- (2008).
 [4] Lui, C. H., Liu L., Mak, K. F., Flynn, G. W., & Heinz, T. F. Ultraflat graphene. *Nature* **462** 339-341 (2009).
 [5] Sutter, P. W., Flege, J. I., & Sutter, E. A. Epitaxial graphene on ruthenium. *Nature Mater.* **7** 406-411 (2008).
 [6] Schmidt, H., Luedtke, T., arthold, P., & Haug, R.J. Mobilities and Scattering Times in Decoupled Graphene

- Monolayers. arXiv:0912.0278.
- [7] de Heer, W. A. *et al.* Epitaxial graphene Solid State Communications **143**, 92-100 (2007).
- [8] First, P. *et al.* Epitaxial Graphenes on Silicon Carbide. MRS Bulliten, to appear April (2010).
- [9] Kim, K. S. *et al.* Large-scale pattern growth of graphene films for stretchable transparent electrodes. Nature **457** 706-710 (2009).
- [10] Kosynkin, D. V. *et al.* Longitudinal unzipping of carbon nanotubes to form graphene nanoribbons. Nature **458** 872-876 (2009).
- [11] Avouris, P., Chen, Z., & Perebeinos, V. Carbon-based electronics. Nature nanotech. **2**, 605-615 (2007).
- [12] Min, H.-K., & MacDonald, A.H. Chiral decomposition in the electronic structure of graphene multilayers. Phys. Rev. B **77**, 155416 (2008).
- [13] Rong, Z. Y., & Kuiper, P. Electronic effects in scanning tunneling microscopy: Moire pattern on a graphite surface. Phys. Rev. B **48**, 17427 (1993).
- [14] Li, Guohong *et al.* Observation of Van Hove singularities in twisted graphene layers, Nature Phys. doi:10.1038/nphys1463.
- [15] Berger, C. *et al.* Ultrathin Epitaxial Graphite: 2D Electron Gas Properties and a Route toward Graphene-based Nanoelectronics. J. Phys. Chem. B **108**, 19912-19916 (2004).
- [16] Hass, J. *et al.* Why Multilayer Graphene on 4H-SiC (0001) Behaves Like a Single Sheet of Graphene. Phys. Rev. Lett. **100**, 125504 (2008).
- [17] Shallcross, S., Sharma, S., Kandelaki, E., & Pankratov, O. A. Electronic structure of turbostratic graphene. arXiv:0910.5811.
- [18] Zhou, S. Y., Gweon, G.-H., & Lanzara, A. Low energy excitations in graphite: the role of dimensionality and lattice defects. Ann. Phys.(N.Y.) **321**, 1730-1746 (2006).
- [19] Lopes dos Santos, J. M. B., Peres, N. M. R., & Castro Neto, A. H. Graphene Bilayer with a Twist: Electronic Structure. Phys. Rev. Lett. **99**, 256802 (2007).
- [20] Shallcross, S., Sharma, S., & Pankratov, O. A. Quantum Interference at the Twist Boundary in Graphene. Phys. Rev. Lett. **101**, 056803 (2008).
- [21] E. McCann and V. I. Falko, Landau-Level Degeneracy and Quantum Hall Effect in a Graphite Bilayer. Phys. Rev. Lett. **96**, 086805 (2006).
- [22] P. Moses and R.H. McKenzie, Comparison of coherent and weakly incoherent transport models for the interlayer magnetoresistance of layered Fermi liquids. Phys. Rev. B **60**, 7998 (1999).
- [23] Zheng, L. & MacDonald, A. H. Tunneling conductance between parallel two-dimensional electron systems. Phys. Rev. B **47**, 10619 (1993).
- [24] L. Zheng and A. H. MacDonald, Tunneling Conductance Between Parallel 2-Dimensional Electron systems. Phys. Rev. B **47**, 10619 (1993) and work cited therein.
- [25] J.P. Eisenstein *et al.*, Probing a 2-Dimensional Fermi-Surface by Tunneling. Phys. Rev. B **44**, 6511 (1991) and work cited therein.
- [26] Miller, D. L. *et al.*, Observing the Quantization of Zero Mass Carriers in Graphene, Science **324**, 924-927 (2009).
- [27] Lyo, S. K. Transport and level anticrossing in strongly coupled double quantum wells with in plane magnetic fields. Phys. Rev. B **50**, 4965 (1994).
- [28] Pereira, V. M., Castro Neto, A. H., & Peres, N. M. R. Tight-binding approach to uniaxial strain in graphene. Phys. Rev. B **80**, 045401 (2009).
- [29] A. B. Kuzmenko, I. Crassee, D. van der Marel, P. Blake, and K. S. Novoselov, Determination of the gate-tunable band gap and tight-binding parameters in bilayer graphene using infrared spectroscopy. Phys. Rev. B **80**, 165406 (2009).
- [30] Lifshitz, R. What is a crystal? Z. Kristallogr. **222**, 313-317 (2007).
- [31] Schmidt, H., Ludtke, T., Barthold, P., & Haug R. J. Mobilities and Scattering Times in Decoupled Graphene Monolayers. arXiv:0912.0278.
- [32] Bonilla, L. L., & Grahm, H. T. Non-linear dynamics of semiconductor superlattices. Rep. Prog. Phys. **68**, 577-683 (2005).
- [33] Bunch J. S. *et al.* Impermeable Atomic Membranes from Graphene Sheets. Nano Lett., **8**, 24582462 (2008).
- [34] See for example W. A. Harrison, *Elementary Electronic Structure* (World Scientific, Singapore, 1999).
- [35] Mahan, G. D., *Many particle physics* (Plenum press, New York, 1990).